The Astrophysical Journal, 609:838–853, 2004 July 10

TWO NEW LOW GALACTIC D/H MEASUREMENTS FROM THE *FAR ULTRAVIOLET SPECTROSCOPIC EXPLORER*[1]

Brian E. Wood,[2] Jeffrey L. Linsky,[2] Guillaume Hébrard,[3,4] Gerard M. Williger,[4] H. Warren Moos,[4] and William P. Blair[4]

Received 2004 February 21; accepted 2004 March 25

ABSTRACT

We analyze interstellar absorption observed toward two subdwarf O stars, JL 9 and LS 1274, using spectra taken by the *Far Ultraviolet Spectroscopic Explorer* (*FUSE*). Column densities are measured for many atomic and molecular species (H I, D I, C I, N I, O I, P II, Ar I, Fe II, and H_2), but our main focus is on measuring the D/H ratios for these extended lines of sight, as D/H is an important diagnostic for both cosmology and Galactic chemical evolution. We find $D/H = (1.00 \pm 0.37) \times 10^{-5}$ toward JL 9 and $D/H = (0.76 \pm 0.36) \times 10^{-5}$ toward LS 1274 (2 σ uncertainties). With distances of 590 ± 160 and 580 ± 100 pc, respectively, these two lines of sight are currently among the longest Galactic lines of sight with measured D/H. With the addition of these measurements, we see a significant tendency for longer Galactic lines of sight to yield low D/H values, consistent with previous inferences about the deuterium abundance from D/O and D/N measurements. Short lines of sight with H I column densities of $\log N(\mathrm{H\ I}) < 19.2$ suggest that the gas-phase D/H value within the Local Bubble is $(D/H)_{\mathrm{LBg}} = (1.56 \pm 0.04) \times 10^{-5}$. However, the four longest Galactic lines of sight with measured D/H, which have $d > 500$ pc and $\log N(\mathrm{H\ I}) > 20.5$, suggest a significantly lower value for the true local disk gas-phase D/H value, $(D/H)_{\mathrm{LDg}} = (0.85 \pm 0.09) \times 10^{-5}$. One interpretation of these results is that D is preferentially depleted onto dust grains relative to H and that longer lines of sight that extend beyond the Local Bubble sample more depleted material. In this scenario, the higher Local Bubble D/H ratio is actually a better estimate than $(D/H)_{\mathrm{LDg}}$ for the true local disk D/H, $(D/H)_{\mathrm{LD}}$. However, if $(D/H)_{\mathrm{LDg}}$ is different from $(D/H)_{\mathrm{LBg}}$ simply because of variable astration and incomplete interstellar medium mixing, then $(D/H)_{\mathrm{LD}} = (D/H)_{\mathrm{LDg}}$.

Subject headings: ISM: abundances — stars: individual (JL 9, LS 1274) — ultraviolet: ISM

1. INTRODUCTION

One of the great successes of the big bang theory is that it predicts the light-element abundances in the universe with reasonable accuracy. However, the exact abundance predictions depend on the cosmic baryon density, Ω_b. The abundance most sensitive to Ω_b is deuterium, so measuring the primordial deuterium-to-hydrogen ratio has become an important method for constraining Ω_b in cosmological models (e.g., Boesgaard & Steigman 1985; Burles et al. 2001). A good estimate of the primordial D/H ratio can be obtained from intergalactic medium (IGM) absorption components seen toward distant quasars, since the metal abundance in the IGM is small, indicating that the gas has experienced very little astration. Kirkman et al. (2003) compile several such measurements (e.g., O'Meara et al. 2001; Pettini & Bowen 2001; Levshakov et al. 2002) and report a primordial D/H of $(D/H)_{\mathrm{prim}} = (2.78^{+0.44}_{-0.38}) \times 10^{-5}$, although there is significant scatter in the individual measurements.[5] This value is consistent with primordial deuterium abundances inferred from recent *WMAP* measurements of the cosmic microwave background, combined with big bang nucleosynthesis calculations (Romano et al. 2003).

Since deuterium is gradually destroyed in the interiors of stars, it is expected that the D/H value should be lower in places that have experienced a lot of stellar processing. Sembach et al. (2004) find a value of $D/H = (2.2 \pm 0.7) \times 10^{-5}$ for Complex C, a high-velocity cloud falling onto the Milky Way, which has a low metallicity but presumably has experienced more stellar processing than most IGM material. The Complex C D/H measurement may be slightly lower than the $(D/H)_{\mathrm{prim}}$ value quoted above, although the uncertainties are too large to provide complete confidence in this result. The D/H ratio in the local disk region of our galaxy, $(D/H)_{\mathrm{LD}}$, should be significantly lower than both the Complex C and IGM measurements as a result of significantly more stellar processing.

Comparing $(D/H)_{\mathrm{LD}}$ to $(D/H)_{\mathrm{prim}}$ provides an excellent indication of the amount of stellar processing experienced by interstellar material in our Galaxy and therefore provides a useful test of Galactic chemical evolution models. Many measurements have been made of the gas-phase local disk D/H ratio in the Galaxy [$(D/H)_{\mathrm{LDg}}$]. These measurements do not account for deuterium that may be locked into molecules and dust, but it has nevertheless been assumed in the past that $(D/H)_{\mathrm{LDg}} \approx (D/H)_{\mathrm{LD}}$. Unfortunately, the D/H measurements for various Galactic lines of sight have not collectively provided an unambiguous value for $(D/H)_{\mathrm{LDg}}$. There seems to be substantial variation in the $(D/H)_{\mathrm{LDg}}$ measurements, at least for longer lines of sight. However, the D/H measurements at least all suggest that $(D/H)_{\mathrm{LDg}} < (D/H)_{\mathrm{prim}}$ as one would expect (e.g., Linsky 1998; Moos et al. 2002).

[1] Based on observations made with the NASA-CNES-CSA *Far Ultraviolet Spectroscopic Explorer* (*FUSE*), which is operated for NASA by Johns Hopkins University under NASA contract NAS5-32985.

[2] JILA, University of Colorado and NIST, Boulder, CO 80309-0440; woodb@origins.colorado.edu, jlinsky@jila.colorado.edu.

[3] Institut d'Astrophysique de Paris, Centre National de la Recherches Scientifique, 98 bis Boulevard Arago, F-75014 Paris, France; hebrard@iap.fr.

[4] Department of Physics and Astronomy, Johns Hopkins University, 3400 North Charles Street, Baltimore, MD 21218; williger@pha.jhu.edu, hwm@pha.jhu.edu, wpb@pha.jhu.edu.

[5] Unless otherwise noted, the quoted uncertainties for averaged quantities are 1 σ standard deviations of the mean, but quoted uncertainties for individual measurements are 2 σ.

Ultraviolet spectra of interstellar H I and D I Lyα absorption lines from the *Hubble Space Telescope* (*HST*) have provided many accurate Galactic D/H measurements (e.g., Linsky et al. 1995; Wood et al. 1996; Dring et al. 1997; Piskunov et al. 1997). However, the D I Lyα line merges with the H I line for H I column densities above $\sim 5 \times 10^{18}$ cm^{-2}. Thus, the *HST* results only apply for short lines of sight with low H I column densities. In particular, the *HST* measurements do not reach beyond the boundaries of the Local Bubble, which is the region within $\sim$100 pc of the Sun in which most of the volume consists of very hot, low-density, ionized interstellar medium (ISM) material (e.g., Snowden et al. 1998; Sfeir et al. 1999; Lallement et al. 2003).

Analogous to the $(D/H)_{LD}$ and $(D/H)_{LDg}$ quantities defined above, we define $(D/H)_{LB}$ and $(D/H)_{LBg}$ to be the total and gas-phase D/H values for the Local Bubble, respectively. Linsky (1998) quotes a value of $(D/H)_{LBg} = (1.5 \pm 0.1) \times 10^{-5}$ based on *HST* measurements of the Local Interstellar Cloud (LIC) immediately surrounding the Sun. This is about a factor of 2 lower than the $(D/H)_{prim}$ value quoted above. More recent measurements from the *Far Ultraviolet Spectroscopic Explorer* (*FUSE*) have confirmed this result (Moos et al. 2002; Oliveira et al. 2003). There is no convincing evidence for D/H variations within the Local Bubble, but $(D/H)_{LBg}$ will equal $(D/H)_{LDg}$ only if interstellar gas in the Galaxy is relatively homogeneous and well mixed. Consideration of longer lines of sight is necessary to determine if $(D/H)_{LDg} = (D/H)_{LBg}$.

Measuring D/H for longer lines of sight requires access to Lyman lines higher than Lyα. Observations of these lines have been provided by the *Copernicus* satellite in the 1970s, the interstellar medium absorption profile spectrograph (IMAPS) instrument (part of the *ORFEUS-SPAS II* experiment on board the STS 80 Space Shuttle *Columbia* flight in 1996), and more recently by *FUSE*, which was launched in 1999. Measurements of D/H from these instruments (e.g., York & Rogerson 1976; Vidal-Madjar et al. 1977; Sonneborn et al. 2000; Hoopes et al. 2003) suggest a significant amount of variability for D/H outside the Local Bubble within the range $D/H = (0.5\text{–}2.2) \times 10^{-5}$ (Moos et al. 2002). When combined with the $(D/H)_{prim}$ measurement, this suggests a deuterium destruction factor of $\sim$1.3–5.6 in the local disk region of the Galaxy. The actual average $(D/H)_{LDg}$ value and the average deuterium destruction factor are presumably somewhere in the middle of the above ranges, but it is not yet clear exactly where.

The spatial variability of the Galactic D/H should disappear if one considers only lines of sight longer than the scale size of the variations, so the longest and highest column density lines of sight should in principle provide the best measurements of $(D/H)_{LDg}$. In practice, however, the high column densities for long Galactic lines of sight often lead to a very confusing spectrum of blended atomic and molecular absorption lines, making identification and accurate measurement of deuterium lines impossible in many cases. Nevertheless, considering D/O and D/N measurements with previously published D/H values, Hébrard & Moos (2003) suggest that the deuterium abundance for long lines of sight is significantly lower than in the Local Bubble. However, there are very few measurements for distances longer than 500 pc. In this paper we double the number of D/H measurements in this distance regime by analyzing *FUSE* observations of two new lines of sight with $d > 500$ pc.

2. THE TARGETS

Our target stars for this project are JL 9, which acquires its name from the catalog of Jaidee & Lyngå (1974), and LS 1274, which acquires its identifier from a catalog of luminous southern hemisphere stars by Stephenson & Sanduleak (1971). The properties of these two stars are listed in Table 1. Both are subdwarf O (sdO) stars. Hot subdwarf stars are excellent targets for our purposes because they provide strong UV continua against which many ISM absorption lines can be seen (including H I and D I lines). They are significantly brighter than white dwarfs and can therefore be used to observe longer lines of sight, but they are not as bright as OB main-sequence stars, which are often too bright to observe with *FUSE*'s sensitive detectors, even at large distances.

TABLE 1
TARGET STAR PROPERTIES

Property	JL 9	LS 1274
Spectral Type	sdO	sdO
R.A. (J2000.0)	19 08 21	09 18 56
Decl. (J2000.0)	−72 30 34	−57 04 38
Galactic longitude (deg)	322.6	277.0
Galactic latitude (deg)	−27.0	−5.3
V	13.2	12.9
$B - V$	−0.28	−0.45
Distance (pc)	590 ± 160	580 ± 100

NOTE.—Units of right ascension are hours, minutes, and seconds, and units of declination are degrees, arcminutes, and arcseconds.

Dreizler (1993) computes a distance of $d = 580 \pm 100$ pc for LS 1274 from spectroscopic analysis, but unfortunately there is no similar measurement for JL 9. A distance for JL 9 can be estimated assuming that it has an absolute magnitude similar to other sdO stars with measured distances. In particular, we use the hot subdwarf catalog of Kilkenny et al. (1988) to identify all sdO stars with $V < 11$ that may be bright and near enough to have reasonably accurate *Hipparcos* distance measurements. We then use the SIMBAD database to determine which stars indeed have *Hipparcos* distances. Only seven stars meet these criteria (CD −31°1701, BD +75°325, Feige 66, HD 127493, HD 149382, BD +28°4211, and BD +25°4655). After adding LS 1274 and its spectroscopic distance to this group, we find an average absolute magnitude of $M_V = 4.40 \pm 0.58$ for this selection of sdO stars. This average sdO magnitude is very similar to the value that Thejll et al. (1997) find for the more numerous sdB stars. Assuming that this is a reasonable estimate for JL 9 yields a distance of $d = 590 \pm 160$ pc, which is the distance reported in Table 1.

3. THE *FUSE* OBSERVATIONS

Table 2 lists the *FUSE* observations used in our analysis. JL 9 was observed once through the low-resolution (LWRS) aperture, while LS 1274 was observed three separate times through the medium-resolution (MDRS) aperture. The JL 9 observation was made in a single 16.6 ks exposure, while the LS 1274 data were taken in 77 separate exposures totaling 85.0 ks.

Hébrard & Moos (2003) have already processed the LS 1274 observations and analyzed them to some extent (see § 4.1). We use the same processed data set. The JL 9 data are processed similarly, using CALFUSE version 2.4.1. The *FUSE* instrument uses a multichannel design to fully cover its 905–1187 Å spectral range: two channels (LiF1 and LiF2) use Al+LiF coatings, two channels (SiC1 and SiC2) use SiC coatings, and there are two different detectors (A and B). For a full description of the instrument, see Moos et al. (2000) and Sahnow

TABLE 2
FUSE Observations

Star	Observation ID	Date	Aperture	Number of Exposures	Exposure Time (ks)
JL 9	P3021201	2003 May 28	LWRS	1	16.6
LS 1274	P2051702	2002 Mar 8	MDRS	11	8.0
	P2051701	2002 Mar 11	MDRS	12	14.0
	P2051703	2002 May 2	MDRS	54	63.0

et al. (2000). With this design *FUSE* acquires spectra in eight segments covering different, overlapping wavelength ranges. For LS 1274, the numerous exposures are cross-correlated and co-added to produce a single spectrum for each segment. For JL 9, this is not absolutely necessary since the observation was taken in a single exposure. However, by first breaking the time-tagged photon address mode observation into 17 subexposures, and then cross-correlating and co-adding the resulting 17 spectra, we found that we could noticeably improve the spectral resolution of the JL 9 data, particularly for the SiC segments. Thus, these are the spectra that are principally used in our analysis.

Although we co-add the individual exposures of the *FUSE* data set, we do not co-add the eight overlapping spectral segments that result from the data reduction, because of concerns that such an operation could significantly degrade the resolution. In Figure 1 we display the full *FUSE* spectrum of JL 9, which is constructed by splicing together the following segments: SiC1B (912–918 Å), SiC2A (918–996 Å), LiF1A (996–1080 Å), SiC2B (1080–1090 Å), and LiF1A (1090–1180 Å). The spectrum is riddled with numerous atomic and H_2 absorption lines from the ISM. The LS 1274 spectrum is quite similar to that of JL 9 shown in Figure 1 and has a similar selection of absorption lines. This is not surprising given that both are sdO stars at roughly the same distance (see Table 1).

There is no wavelength calibration lamp on *FUSE*, so determining the absolute wavelength scale can be difficult. We use the numerous H_2 lines seen throughout the spectrum as wavelength calibration lines to ensure that the full spectrum is on a self-consistent relative wavelength scale. In other words, we calibrate the wavelengths to ensure that all H_2 lines are centered on the same velocity. For JL 9, the implied wavelength corrections are relatively uniform across the individual spectral segments, so a single wavelength correction factor is used for each entire segment. However, for LS 1274 the wavelength corrections implied by the H_2 lines vary significantly (up to $\sim$5 km s^{-1}) within several of the segments, forcing us to use variable correction factors across the segments. For the *absolute* wavelength calibration, we force the H_2 line velocities to agree with the average H_2 line velocity seen within the LiF1A segment. We choose LiF1A to establish the absolute wavelength scale because the LiF1 channel is used for target guiding, meaning that the target should be most accurately centered in the aperture for the LiF1A and LiF1B segments, and those segments should therefore have the best absolute wavelength scales.

Geocoronal airglow emission is observed within the strongest of the broad H I lines (e.g., H I Lyβ, Lyγ, and Lyδ at 1025.7, 972.5, and 949.7 Å, respectively). This emission is naturally stronger in the JL 9 spectrum, since those data were taken through the LWRS aperture rather than the narrower MDRS aperture. Fortunately, for both stars the airglow lines are roughly centered in the saturated cores of the broad H I absorption lines, so the emission can be subtracted with reasonable accuracy. Figure 1 shows the JL 9 data after this subtraction has already been performed. Nevertheless, for JL 9 there may be flux inaccuracies near the short-wavelength side of the H I Lyγ and Lyδ lines due to uncertainties in the airglow removal. No attempt is made to correct for O I and N I airglow emission. However, this emission is potentially a problem for only a small number of lines and probably not a problem at all for the MDRS LS 1274 data. Nevertheless, the excess emission in the bottom of the JL 9 O I absorption feature at 988.4 Å in Figure 1 is surely airglow emission.

4. ANALYSIS

4.1. *Profile Fitting Procedures*

Figure 1 shows that the *FUSE* spectra contain numerous interstellar lines of 13 different atomic species and a forest of H_2 lines from rotational levels $J = 0$–5. The primary goal in analyzing these data is to extract accurate column densities from these absorption lines for all of the atomic and molecular species represented in the spectra. The final results are listed in Table 3, and we describe below the profile fitting methods used to measure these column densities and 2 σ uncertainties. Note that Table 3 does not list column densities for C II, C III, N II, N III, and Si II. There are lines of these species in the spectra, and they are even included in the fit in Figure 1, but we do not believe that we can derive reliable column densities from these lines. There are several reasons for this. One is that each of these species is represented by only one or two highly saturated lines in the flat part of the curve of growth that cannot yield precise column density measurements. The C II, N III, and Si II lines are also highly blended with other lines. Finally, we are concerned about the possibility of stellar absorption contaminating the interstellar C II, C III, N II, and N III lines, especially for LS 1274.

Our primary approach to measuring column densities is to perform global fits to the absorption lines, like the fit shown in Figure 1. In this approach, a spectrum covering the full *FUSE* spectral range is constructed from the *FUSE* segments, as described in § 3, and all the lines in the spectrum are then fitted simultaneously. This approach has been previously used to analyze the lines of sight to WD 1634−573 and WD 2211−495 (Wood et al. 2002; Hébrard et al. 2002). However, as in these two previous cases, we also perform an independent analysis using the Owens.f profile fitting code, which was developed by the French *FUSE* team and has been used extensively for measuring ISM lines in *FUSE* observations of other targets (Friedman et al. 2002; Kruk et al. 2002; Lehner et al. 2002; Lemoine et al. 2002; Sonneborn et al. 2002; Hébrard & Moos 2003; Hoopes et al. 2003; Oliveira et al. 2003).

Column density measurements from absorption lines are susceptible to many systematic errors: continuum placement

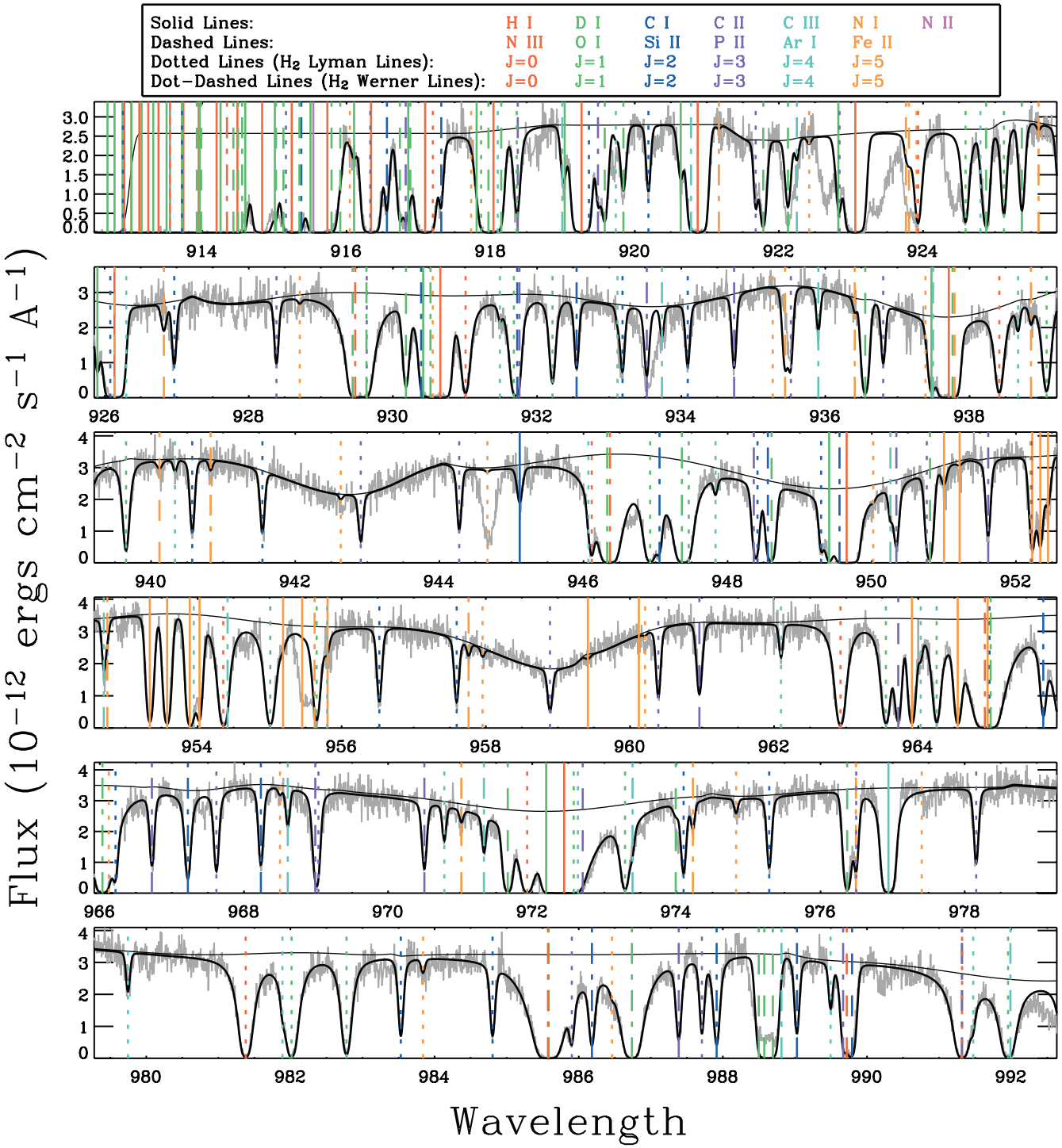

FIG. 1.—*FUSE* spectrum of JL 9 and a fit to the ISM absorption lines seen in the spectrum. Vertical lines of various types and colors indicate the locations of ISM absorption lines included in the fit, where a key at the top of the figure identifies the lines. The H_2 lines are separated into Lyman band lines and Werner band lines.

issues, unresolved velocity structure, unidentified blends, uncertain instrumental line profile, etc. Performing two independent and very different analyses allows us to see whether different assumptions and methods still lead to similar measurements. This ultimately increases confidence in our final results. The Owens.f analysis provides column density measurements for the important D I, O I, N I, and Fe II species, so the column densities reported in Table 3 for these species are compromises between the results of the two independent analyses. The Owens.f analysis for LS 1274 has already been reported by Hébrard & Moos (2003), and we refer the reader to that paper for details. A very similar analysis is performed on the JL 9 data, but we focus here mostly on the global fitting method.

The first step in performing a global fit to a spectrum like that in Figure 1 is to estimate the stellar continuum. This is initially done with the help of a polynomial fitting routine to extrapolate over the absorption lines, although the continuum is refined after initial fits to the data in order to improve the quality of the fit. We do not try to compute synthetic model

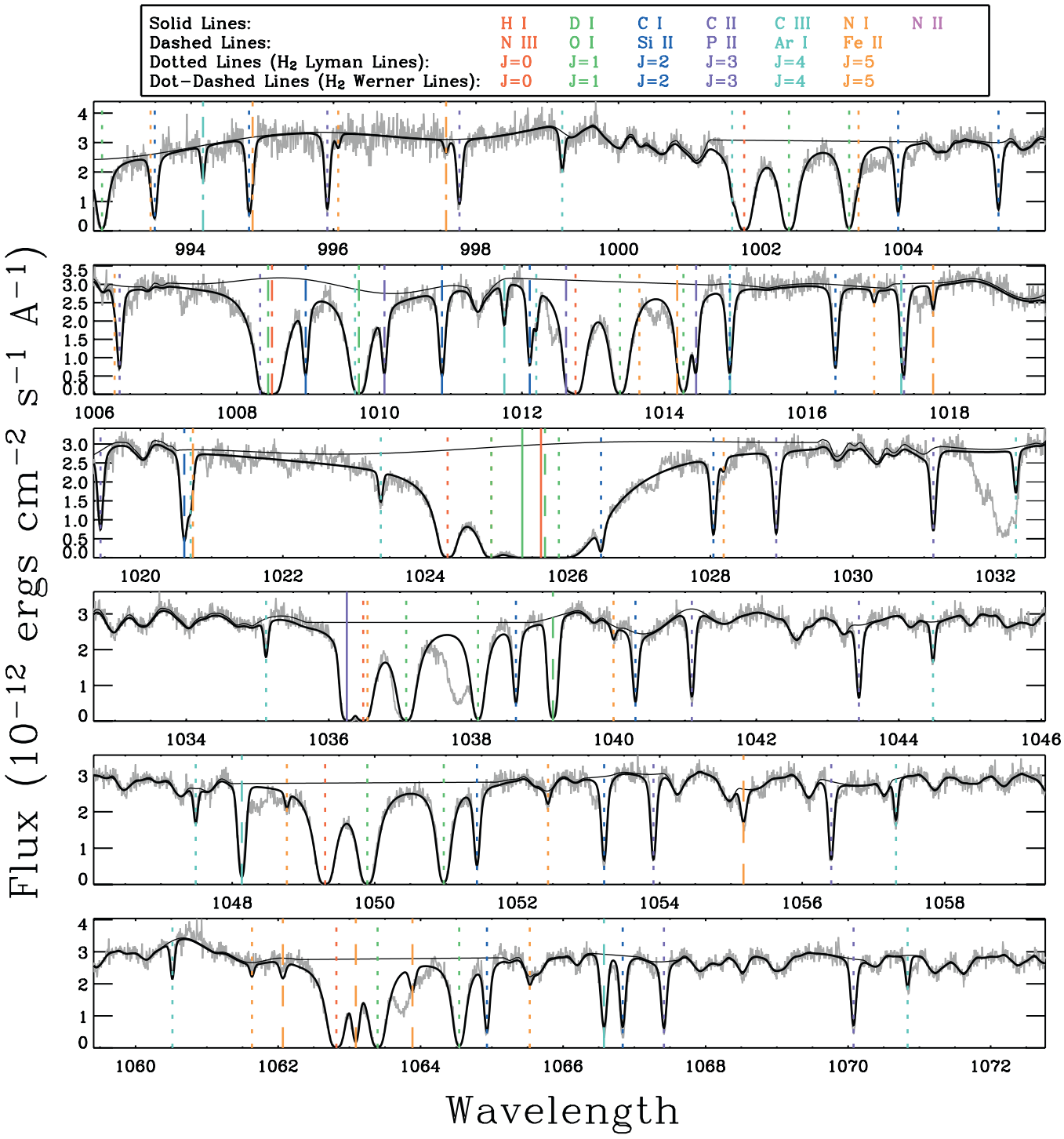

FIG. 1.—*Continued*

continua for these stars because their stellar parameters are poorly known (especially JL 9) and because such models are of limited accuracy in matching observations (e.g., Friedman et al. 2002). The entire spectrum and all the ISM absorption lines within it are fitted simultaneously. We use the Morton (2003) list of atomic lines as our source for all necessary atomic data. We include in our fit all reasonably strong lines of the 13 atomic species with at least one detected line (see Fig. 1). This includes not only lines that are clearly detected but many undetected lines as well, since nondetections can also provide constraints for the fit. We use the Abgrall et al. (1993a, 1993b) lists of Lyman and Werner band H_2 lines to fit the H_2 absorption. We include all $v = 0, J = 0$–5 transitions in the fit, once again including both detected and undetected lines. The final tally of lines included in the fit is 140 atomic and 312 H_2 lines. Their locations are shown in Figure 1.

The three parameters of any absorption-line fit are the line centroid velocity (v), the column density (N), and the Doppler broadening parameter (b). In our fits, all lines of a given atomic species are naturally forced to have the same column density. The atomic lines are also forced to have the same centroid velocities, except for H I. The H I lines are much

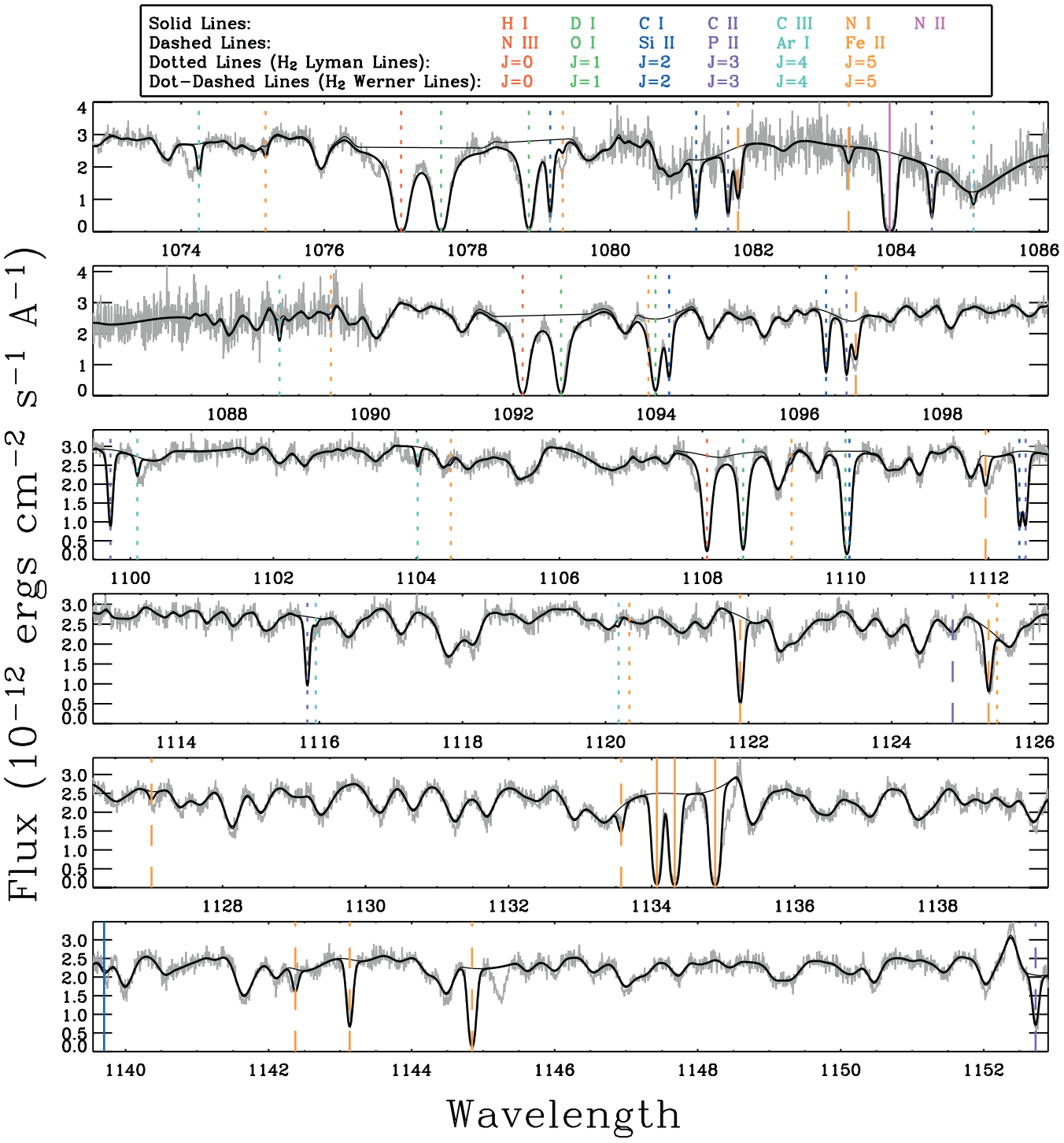

FIG. 1.—*Continued*

stronger than the other lines and are therefore sensitive to weaker ISM velocity components. They clearly have a different centroid velocity because of this, so in the fits the H I lines are allowed to have their own independent velocity. The Doppler parameter (in km s^{-1}) is related to the temperature (T) and nonthermal velocity (ξ) of the ISM gas by $b^2 = 0.0165T/A + \xi^2$, where A is the atomic weight of the species in question. In our fits, we use T and ξ as free parameters and compute b-values for all atomic lines from these parameters. In this way, the fits to all individual atomic lines and the fit parameters are in some sense interdependent. However, the H I lines are once again treated separately and allowed to have their own independent b-value. The H_2 lines are surely formed in different, cooler regions of the ISM than the atomic lines, so their velocities and Doppler parameters are allowed to be different from those of the atomic lines. All H_2 lines of a given rotational level are naturally forced to have the same column density.

Spectral regions that are heavily contaminated by stellar absorption are ignored in the fits. Examples in Figure 1 include the 922.0–924.5, 933.3–933.9, 944.5–945.0, 955.3–955.6, 1031.5–1032.5, and 1037.5–1038.0 Å regions, which

TABLE 3
Measured Column Densities

Species	log N[a] (cm^{-2}) JL 9	LS 1274
H I	20.78 ± 0.10	20.98 ± 0.08
D I	15.78 ± 0.12	15.86 ± 0.18
C I	13.49 ± 0.16	13.55 ± 0.16
N I	16.27 ± 0.20	16.52 ± 0.36
O I	17.50 ± 0.33	17.65 ± 0.15
P II	13.67 ± 0.20[b]	13.66 ± 0.23[b]
Ar I	14.48 ± 0.20[b]	14.49 ± 0.35[b]
Fe II	14.69 ± 0.17	14.81 ± 0.15
$H_2(J = 0)$	18.87 ± 0.04	18.88 ± 0.05
$H_2(J = 1)$	18.99 ± 0.04	18.67 ± 0.07
$H_2(J = 2)$	17.56 ± 0.31[b]	17.32 ± 0.50[b]
$H_2(J = 3)$	17.37 ± 0.43[b]	16.85 ± 0.83[b]
$H_2(J = 4)$	14.76 ± 0.14	14.54 ± 0.16
$H_2(J = 5)$	14.02 ± 0.27	13.83 ± 0.29
H_2(total)	19.25 ± 0.03	19.10 ± 0.04

[a] With 2 σ uncertainties.
[b] Potentially unreliable as a result of measurement solely from saturated lines in the flat part of the curve of growth.

are contaminated by stellar absorption lines of N IV, S VI, and O VI. We also ignore the region around the O I λ988 line since it is contaminated by airglow emission (see § 3).

The spectral resolution of *FUSE* is not sufficient to resolve narrow ISM absorption lines, so a fit to the data must be convolved with the instrumental line-spread function (LSF) before being compared to the data. Unfortunately, the *FUSE* LSF is not well known (Kruk et al. 2002). It varies with wavelength, it can vary from one observation to the next, and it can also depend on exactly how the data are processed (see § 3). For these reasons, the LSF is generally a free parameter of our fits, where we assume a double-Gaussian representation for the LSF. However, we make no attempt to correct for variations of the LSF with wavelength, which is a potential source of systematic error in the analysis. Wood et al. (2002) derived an average *FUSE* LSF from various fits to *FUSE* spectra. We experiment with simply using that LSF in our analysis, although we find that the LSFs of our spectra are somewhat narrower than this, especially for the LS 1274 data.

Figure 1 shows one fit to the JL 9 data, but ultimately a large number of fits are considered before estimating best values and uncertainties for the ISM column densities. For example, we experiment with different continuum estimations. This is done in several different ways, but the simplest is to arbitrarily increase or decrease the entire continuum by various percentages to see if the fits to the various absorption lines still look reasonable and to see how much the derived column densities change as a consequence of the continuum variation. As mentioned above, we also experiment with using the LSF from Wood et al. (2002) rather than allowing the LSF to vary.

Although we generally work with *FUSE* spectra constructed from the individual *FUSE* segments as described in § 3, we also try using the SiC1B segment to cover the entire region below 990 Å instead of using SiC2A. The extra attention to this spectral region is warranted since all of the important D I, N I, and O I lines are located below 990 Å.

Most of the observed N I and O I lines are saturated and lie in the flat part of the curve of growth. In order to make sure that including these lines in the fit is not leading to column densities radically different from those suggested by the optically thin lines, we experiment with fits in which the saturated N I and O I lines are ignored.

Finally, we also experiment with two-component fits to the data rather than single-component fits. Unfortunately, *FUSE* does not have sufficient resolution to assess the velocity structure of the ISM along our two lines of sight, and no other high-resolution observations of JL 9 or LS 1274 exist that can assist us in this matter. This lack of knowledge of the ISM structure is a potentially significant source of systematic error, so we try fits to the data with two components to test whether these fits result in significantly different column densities. For example, we try fits with components that have a velocity separation of 10 km s^{-1} and a column density difference in all lines of 0.5 dex.

The idea behind all this experimentation is to collect a large number of acceptable fits to the data with different assumptions, and then for each column density in question we use the range of values suggested by this set of fits to define the best value and its uncertainty. Uncertainties derived in this fashion are not statistical in nature, but we believe they can be considered approximately 2 σ errors, in the sense of representing roughly 95% confidence intervals. The uncertainties are certainly larger than 1 σ since we do not throw out 32% of our acceptable fits in estimating the errors.

As mentioned above, the results of the global fits are compared with those of the Owens.f code (at least for D I, N I, O I, and Fe II), and the final column densities and uncertainties reported in Table 3 are essentially averages of the two independent measurements. The two analyses yield column densities that generally agree very well. The only exception is the N I column density for LS 1274, which is discussed in § 4.3.4. The Owens.f analysis represents a significantly different approach to fitting the data in terms of line selection, continuum estimation, LSF treatment, and uncertainty derivation (see Hébrard et al. 2002; Hébrard & Moos 2003). Thus, ensuring that the column density values reported here are consistent with both analyses significantly improves our confidence in these results.

4.2. *Velocities and Doppler Parameters*

In the global fits described in § 4.1, the ISM absorption lines are divided into three categories: atomic lines, H I lines, and H_2 lines. The heliocentric centroid velocities of these lines in the JL 9 fit in Figure 1 are −24.2, −29.2, and −17.2 km s^{-1} for the atomic, H I, and H_2 lines, respectively. These values are of questionable accuracy as a result of the uncertainty in the absolute wavelength scale (see § 3), but these velocities are not too different from the ISM velocity expected for the LIC along this line of sight. The LIC vector of Lallement et al. (1995) predicts a line of sight velocity of −12.6 km s^{-1}, which is not too far away from the measured velocities listed above considering that multiple ISM components will certainly exist along this lengthy line of sight that will shift the measured line centroids away from the LIC velocity. Similar rough agreement is found for LS 1274, where the predicted LIC velocity is 0.3 km s^{-1} and the measured velocities are 4.2, 5.9, and 9.2 km s^{-1} for the atomic, H I, and H_2 lines, respectively.

In the global fits, Doppler parameters of the atomic lines are computed from T- and ξ-values, which are free parameters of the fits. Since the lines are not resolved and we do not know the ISM velocity structure along the lines of sight, the meaning of these parameters is very questionable. In all of the fits, the b-values are dominated by the nonthermal broadening

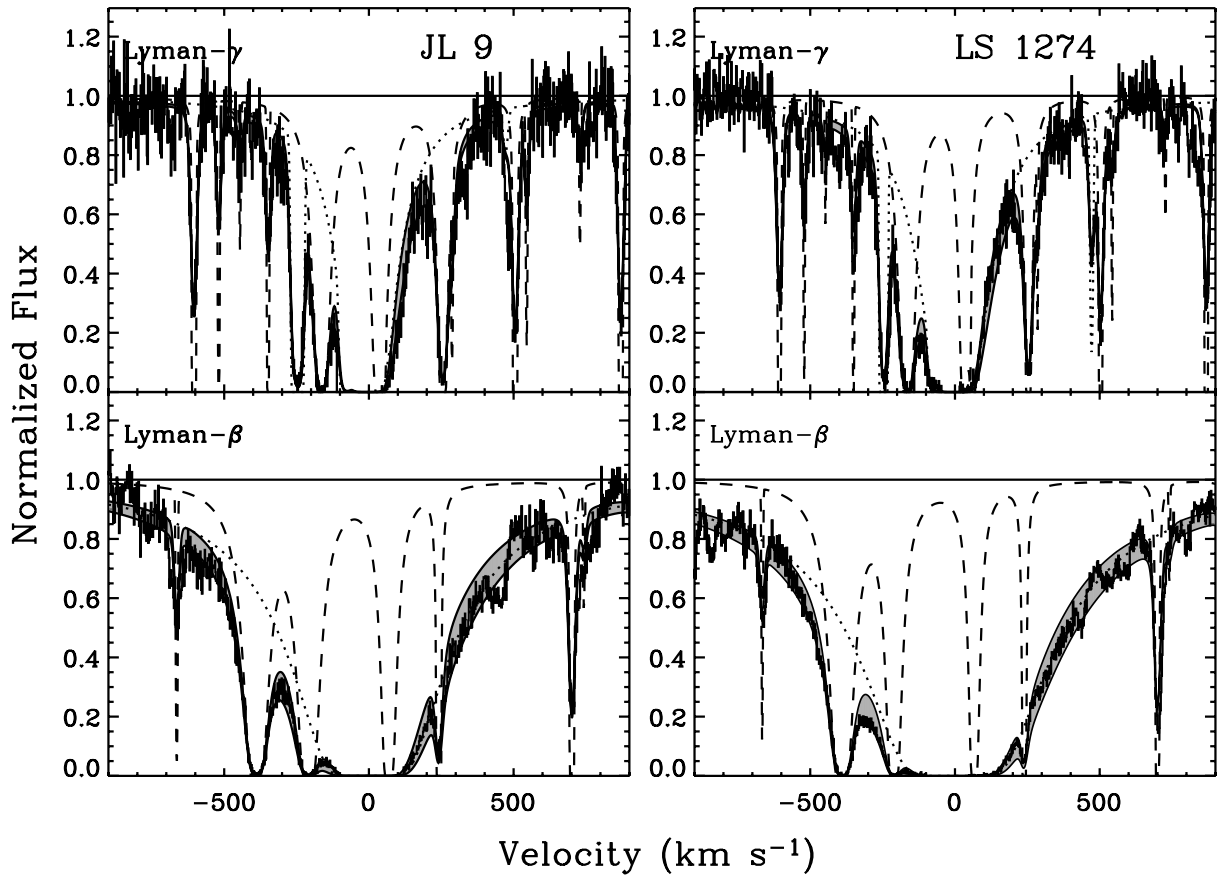

FIG. 2.—H I Lyβ and Lyγ lines of JL 9 and LS 1274, which are the only H I lines that have substantial damping wings that can be used to measure an accurate H I column density. Fits to the data are shown, which are actually part of global fits like that in Fig. 1. The dotted line in each panel is the absorption from all the atomic lines (including H I and D I), and the dashed line is the H_2 absorption, both lines shown prior to convolution with the instrumental LSF. The shaded region shows the range of profile fits after convolution, defined by the ± 2 σ range of acceptable H I column densities listed in Table 3.

parameter (ξ). We find $\xi \approx 11$ km s^{-1} for JL 9 and $\xi \approx 6$ km s^{-1} for LS 1274. The H I lines also show larger line widths for the JL 9 line of sight, where we typically find b(H I) ≈ 15 km s^{-1} for JL 9 compared with b(H I) ≈ 13 km s^{-1} for LS 1274. The larger ξ- and b-values for the JL 9 line of sight may imply a broader distribution of ISM velocity components, at least for the atomic lines. In contrast, we typically find $b(H_2) \approx 3$ km s^{-1} for both lines of sight.

4.3. *Column Densities*

The most important fit parameters are the column densities. The accuracy of a column density measurement depends on where the set of available lines is on the curve of growth (see, e.g., Spitzer 1978). Optically thin lines in the linear part of the curve of growth provide the best constraints on the column densities, although weak lines are more sensitive to errors induced by low signal-to-noise ratio, unidentified blends, and uncertainties in continuum placement. Excellent constraints on the column density are also provided by very strong lines with damping wings, which are in the square root part of the curve of growth (i.e., H I Lyβ and most of the H_2 $J = 0$–1 lines), although extrapolating an accurate continuum over these very broad lines can be problematic. Intermediate saturated lines without damping wings in the flat part of the curve of growth are not very sensitive diagnostics for column densities. Column densities derived solely from these lines can be very sensitive to certain assumptions involved in any fit, e.g., how Doppler parameters and instrumental LSFs are treated (see Hébrard et al. 2002). Thus, these column densities are flagged in Table 3 as being potentially unreliable. The individual column density measurements and the lines from which they are derived are now discussed in detail.

4.3.1. *Hydrogen*

There are a large number of H I lines in the *FUSE* spectra (see Fig. 1), but most are highly saturated and located on the flat part of the curve of growth. The exceptions are the two strongest lines, Lyβ at 1025.7 Å and Lyγ at 972.5 Å, which are shown in Figure 2. Our derivation of precise H I column densities relies on the existence of substantial damping wings for these lines, especially for Lyβ. The figure shows the spread of fits suggested by the ± 2 σ error bars in the H I column densities quoted in Table 3. Figure 2 illustrates the importance of correcting for the strong H_2 absorption along the blue sides of both the Lyβ and Lyγ lines. Since Lyβ and Lyγ have damping wings, the Lyα line at 1216 Å surely does as well. The Lyα line is not accessible to *FUSE*, but the *International Ultraviolet Explorer* (*IUE*) observed this line for JL 9 in 1984. From these data, Diplas & Savage (1994) derived a value of $\log N(\mathrm{H\ I}) = 20.79 \pm 0.14$ for JL 9. This agrees very well with our $\log N(\mathrm{H\ I}) = 20.78 \pm 0.10$ result from the better quality *FUSE* data. Unfortunately, there are no *IUE* or *HST* observations of the Lyα line of LS 1274.

4.3.2. *Deuterium*

Located -82 km s^{-1} from every H I Lyman line is a D I Lyman line. Figure 3 shows the D I lines that provide the best

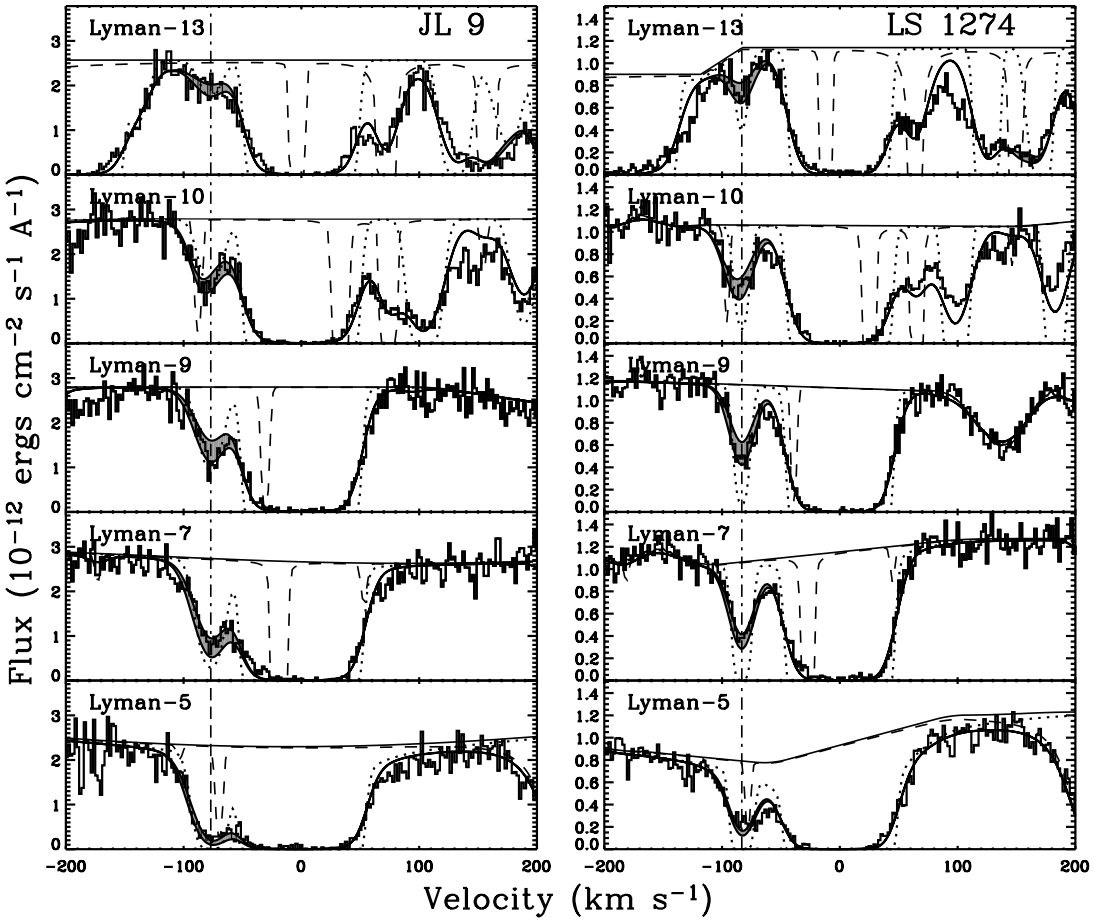

FIG. 3.—Close-up of all useful D I lines (*dot-dashed line*) in the *FUSE* spectra of JL 9 and LS 1274, plotted on a velocity scale centered on the H I lines bordering D I. Fits to the data are shown, which are actually part of global fits to the full spectra, as in Fig. 1. The dotted line in each panel is the absorption from all the atomic lines (including H I and D I), and the dashed line is the H_2 absorption, both lines shown prior to convolution with the instrumental profile. The shaded region shows the range of profile fits after convolution, defined by the ± 2 σ range of acceptable D I column densities listed in Table 3.

constraints on the D I column density and shows the spread of fits suggested by the ± 2 σ error bars in the D I column densities quoted in Table 3. All other D I lines are either saturated and highly blended with H I or heavily blended with other strong ISM absorption lines that happen to lie near them (see Fig. 1). Even for the Ly5 and Ly10 lines in Figure 3 there are weak H_2 blends that must be taken into account in fitting these lines. The LS 1274 D I measurement in Table 3, $\log N(\mathrm{D\ I}) = 15.86 \pm 0.18$ (2 σ error), is in excellent agreement with the $\log N(\mathrm{D\ I}) = 15.87 \pm 0.10$ (1 σ error) result from Hébrard & Moos (2003) based on only the Owens.f analysis.

The H I, D I, and O I lines become increasingly crowded below 930 Å, in addition to the ever-present H_2 lines (see Fig. 1). The Ly13 D I line at 916.2 Å is the highest D I Lyman line that has ever been detected, although it has also been observed and measured previously for Feige 110, HD 195965, and HD 191877 (Friedman et al. 2002; Hoopes et al. 2003). Figure 1 suggests that this may be the highest D I Lyman line that one can *ever* hope to clearly detect, since absorption from H I, O I, N II, and H_2 will probably always obscure higher D I lines at shorter wavelengths. The D I Ly13 line will become saturated for column densities of $\log N(\mathrm{D\ I}) \gtrsim 16.5$, so measuring a precise D I column density for lines of sight with higher columns will be impossible. Our measured D I column densities listed in Table 3 are only about a factor of 4 below this limit. Thus, our two targets are near the high column density limit where direct D/H measurements are still possible. Beyond this limit, the only way to measure D/H is through deuterated molecular lines, but interpretation of these lines requires detailed chemical modeling (Lubowich et al. 2000).

4.3.3. *Oxygen*

A large number of O I lines exist in our spectra (see Fig. 1), but all but one are saturated and located on the flat part of the curve of growth. The one exception is the O I line at 974.07 Å, which is blended with two H_2 lines. Because of the importance of the O I λ974.07 line in deriving a precise O I column density, we try fitting it alone, as well as including it in the global fits. These fits are shown in Figure 4 for both the SiC2A and SiC1B segments. Although these fits are not part of global fits, the results of the global fits are used to constrain the centroids and Doppler parameters of the O I and blended H_2 lines and are also used to determine the assumed LSFs. Note the significantly lower resolution of the SiC1B data in this wavelength region for both stars.

For LS 1274, the O I column densities suggested by the two fits in Figure 4 are nicely consistent with the results from the global fits. However, this is not the case for JL 9, at least for the SiC2A data. The global JL 9 fits lead to very poor fits to the SiC2A O I λ974.07 line. Even the SiC2A JL 9 fit in Figure 4 does not look very good, although the combined fit to O I and

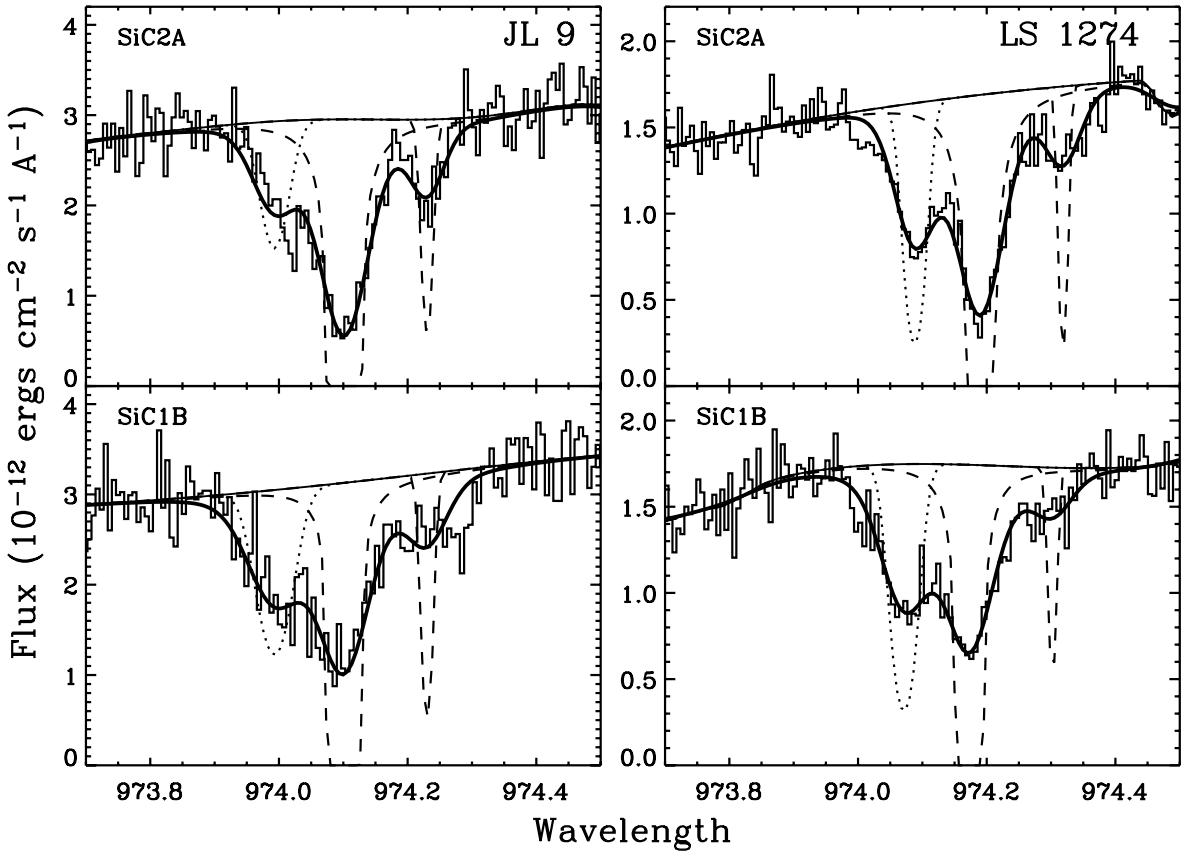

FIG. 4.—Fits to the blended O I λ974.07, $H_2(J = 2)$ λ974.16, and $H_2(J = 5)$ λ974.28 lines. The dotted (O I) and dashed (H_2) lines show the individual absorption components, and the thick solid lines show the total absorption after convolution with the instrumental profile. The fits are shown for both the SiC2A and SiC1B segments.

the two H_2 lines has a reasonable $\chi^2_\nu = 1.10$ value. The observed O I absorption seems to be too redshifted and too blended with the H_2 absorption. The reason for this is unclear, but we decide that for JL 9 the results of the O I fits in Figure 4 lead to better fits and more believable O I column densities than the global fits (at least for the SiC2A data). Thus, the Figure 4 fits are the primary source of the JL 9 O I column density reported in Table 3, in addition to the Owens.f results. Note that the LS 1274 O I measurement in Table 3, $\log N(\mathrm{O\ I}) = 17.65 \pm 0.15$ (2 σ error), is in perfect agreement with the $\log N(\mathrm{O\ I}) = 17.62 \pm 0.08$ (1 σ error) result from Hébrard & Moos (2003) based on only the Owens.f analysis.

Since charge exchange should keep O and H in the same ionization state in the ISM, O I has been used as a proxy for H I in cases in which H I cannot be measured accurately, and D/O has been used as a proxy for D/H (see Hébrard & Moos 2003). However, in the high column density regime in which our two lines of sight exist, H I can be measured more accurately than O I (see Table 3). This is because the high column densities lead to almost all of the O I diagnostics being saturated but also lead to strong damping wings for H I Lyβ, which provide excellent constraints on the H I column (see § 4.3.1).

4.3.4. *Nitrogen*

The primary constraints on the N I column density are the N I lines between 950 and 965 Å (see Fig. 1). The LS 1274 N I column density measured from these lines is the only column density in which the global fits and the Owens.f analysis are not in good agreement. The Owens.f analysis focuses only on the optically thin lines, which should provide the best constraints. This analysis therefore relies on the N I $\lambda\lambda$951.08, 951.29, 955.52, 955.88, and 959.49 lines (Hébrard & Moos 2003). However, in the global fits the absorption features near the $\lambda\lambda$951.29 and 959.49 lines are seen to be shifted significantly from the expected positions of the N I absorption and are therefore essentially ignored. The stronger N I λ952.52 line, which is not considered in the Owens.f analysis, seems to suggest lower column densities than the weaker lines mentioned above. The global fits are driven to fit this and other strong N I lines well instead of fitting the weak lines well. The λ955.88 line is blended with an H_2 line, complicating its analysis, and it is only in the SiC1B data that there is a weak feature that might be N I λ955.52; it is not apparent in SiC2A. In short, in the global fits some (possibly all) weak lines used in the Owens.f analysis are seen as being contaminated by blends or continuum variations. On the other hand, all the strong lines used in the global fit (except maybe λ952.52) are saturated, which makes the column density measurements from the global fits subject to systematic effects due to the unknown velocity structure of the line of sight and the unknown shape of the LSF (Hébrard et al. 2002). In addition, many of the strong N I lines are blended, complicating their analysis.

The results of the global fit and the Owens.f fits are $\log N(\mathrm{N\ I}) = 16.30 \pm 0.28$ and 16.73 ± 0.10, respectively. It is difficult to be sure which of these two analyses gives a more reliable answer, so the N I column density listed in Table 3, $\log N(\mathrm{N\ I}) = 16.52 \pm 0.36$, is a compromise value and the

assumed error bar is expanded to encompass the 1 σ error ranges suggested by both analyses. This leads to a larger uncertainty than one would expect for an atomic species with a seemingly good selection of absorption lines. Nevertheless, this illustrates the wisdom of considering two independent analyses in deriving our column densities, since the two approaches can reveal potential problems and systematic errors that would otherwise be unrecognized.

4.3.5. *Other Atomic Lines*

The measured column densities in Table 3 yet to be discussed are those of C I, P II, Ar I, and Fe II. The C I measurements are entirely based on the C I λ945.19 line, which is not saturated and therefore provides a reasonably accurate C I column. There are a large number of Fe II lines in the spectra, including many unsaturated ones (see Fig. 1), but several of these lines are not fitted well (e.g., the $\lambda\lambda$926.21, 926.90, and 1142.47 lines). The nature of the discrepancy is the same for both our lines of sight, so we suspect inaccurate oscillator absorption strengths for these lines, and such inaccuracies could be significant sources of systematic uncertainty for the Fe II column densities. Howk et al. (2000) have previously found significant problems with a few other Fe II lines in the *FUSE* bandpass, although not the ones mentioned above.

The Ar I column density is derived from two lines at 1048.22 and 1066.66 Å, and the P II column density is measured from detected lines at 961.04, 963.80, and 1152.82 Å. Unfortunately, the Ar I and P II lines are all saturated and located on the flat part of the curve of growth, meaning that our column density measurements must be considered to be potentially unreliable, as discussed above, despite our efforts to be particularly conservative regarding uncertainty estimates.

4.3.6. *Molecular Hydrogen*

Figure 1 shows that absorption lines of molecular hydrogen are ubiquitous throughout the *FUSE* spectra of JL 9, as they are for LS 1274 as well. The H_2 lines actually outnumber the detected atomic lines. Nearly all of the numerous $H_2(J = 0)$ and $H_2(J = 1)$ lines have strong damping wings. This leads to particularly precise column density measurements for these two H_2 levels, which have smaller error bars than any of our other measurements (see Table 3). In contrast, the $H_2(J = 2)$ and $H_2(J = 3)$ lines are all saturated and in the flat part of the curve of growth. Despite the existence of a large number of such lines, we still find large error bars for the column densities of these H_2 levels. Error bars are lower for the $H_2(J = 4)$ and $H_2(J = 5)$ column densities, since there are optically thin H_2 lines in the *FUSE* spectra that provide better constraints.

We are able to measure column densities for the six lowest H_2 levels, and in Figure 5 we plot the relative level populations for both the JL 9 and LS 1274 lines of sight. The populations are very similar for these two cases. Figure 5 also illustrates thermal populations for $T = 50$–200 K, demonstrating that the observed level populations are not well represented by a single thermal population. This is typical for interstellar H_2. The usual explanation for this is that the $J \geq 2$ levels are nonthermally populated by radiative de-excitation from high levels, which are pumped by UV photons (e.g., Black & Dalgarno 1973; Snow et al. 2000; Rachford et al. 2001). Despite these nonthermal effects, the $H_2(J = 1)/H_2(J = 0)$ column density ratio is generally assumed to be indicative of the actual thermal temperature of the H_2 gas. This ratio suggests temperatures of $T = 89 \pm 6$ and 64 ± 5 K for JL 9 and LS 1274, respectively. These values are consistent with the $T = 77 \pm 17$ K average ISM H_2 temperature found by Savage et al. (1977) for 61 lines of sight observed by *Copernicus* and with the average temperature of $T = 68 \pm 15$ K measured by Rachford et al. (2002) for 23 lines of sight observed by *FUSE*.

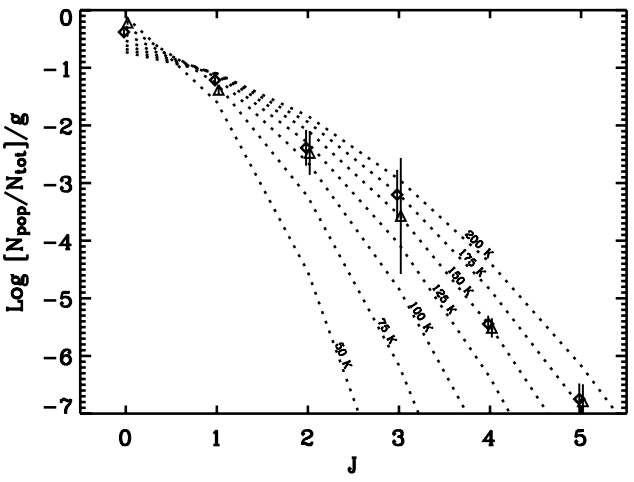

FIG. 5.—Relative H_2 level populations (normalized by the statistical weight g) for the JL 9 (*diamonds*) and LS 1274 (*triangles*) lines of sight. Also shown are curves indicating thermal populations for temperatures of 50–200 K.

The total H_2 column densities toward JL 9 and LS 1274 are $\log N(H_2) = 19.25 \pm 0.03$ and 19.10 ± 0.04, respectively. The hydrogen molecular fraction can be defined as $f(H_2) = 2N(H_2)/[2N(H_2) + N(H\ I)]$. We find low molecular fractions of $f(H_2) = 0.056 \pm 0.012$ and 0.032 ± 0.006 for the JL 9 and LS 1274 lines of sight, respectively.

5. THE GALACTIC D/H RATIO

5.1. *A Revised Galactic Gas-Phase* D/H *Estimate*

The quantity that we are most interested in measuring for our two lines of sight is the interstellar gas-phase D/H ratio. Based on the H I and D I column densities listed in Table 3, we find that $D/H = (1.00 \pm 0.37) \times 10^{-5}$ for JL 9 and $D/H = (0.76 \pm 0.36) \times 10^{-5}$ for LS 1274 (2 σ uncertainties). The molecular fraction for these lines of sight is very low (see § 4.3.6), so these atomic D/H ratios should be excellent measurements of the gas-phase D/H ratio.

In order to place these new measurements into their proper context, we have compiled a large number of D/H measurements for comparison. These D/H values are listed in Table 4. Previous lists of D/H measurements from McCullough (1992), Linsky (1998), and Moos et al. (2002) were invaluable in compiling Table 4, but the references in the table are to the original sources. The list is meant to be as comprehensive as possible, but D/H values with extremely large uncertainties (i.e., greater than a factor of 2) are not listed, and we only list the most recent D/H measurements for each line of sight. Many of the older *Copernicus* measurements have been superseded by better observations and analyses. *Hipparcos* distances are used when available, but some of the distances are simply those quoted in the references. The "Satellite" column in Table 4 identifies the source of the D I measurement, although for G191-B2B and HZ 43 observations of D I Lyα from *HST* were considered in addition to the *FUSE* data.

The error bars on the D/H values in Table 4 are assumed to be 1 σ. Deciding how to interpret the error bars given in the literature can be difficult. Some analyses quote uncertainties as

TABLE 4
COMPILATION OF D/H MEASUREMENTS

Target	l (deg)	b (deg)	d (pc)	log N(H I)[a]	D/H[a] (10^{-5})	Satellite	Flag[b]	References
ϵ Eri	227	−48	3.218 ± 0.009	17.880 ± 0.035	1.4 ± 0.2	*HST*	LBg	1
Procyon	214	13	3.50 ± 0.01	18.06 ± 0.05	1.6 ± 0.2	*HST*	LBg	2
ϵ Ind	336	−48	3.626 ± 0.009	18.00 ± 0.05	1.6 ± 0.2	*HST*	LBg	3
36 Oph	358	7	5.99 ± 0.04	17.850 ± 0.075	1.50 ± 0.25	*HST*	LBg	4
β Gem	192	23	10.34 ± 0.09	18.261 ± 0.037	1.47 ± 0.20	*HST*	LBg	1
Capella	163	5	12.9 ± 0.1	18.239 ± 0.035	$1.60^{+0.14}_{-0.19}$	*HST*	LBg	2
β Cas	118	−3	16.7 ± 0.1	18.130 ± 0.025	1.70 ± 0.15	*HST*	LBg	1
α Tri	139	−31	19.7 ± 0.3	18.327 ± 0.035	1.32 ± 0.30	*HST*	LBg	1
λ And	110	−15	25.8 ± 0.5	18.45 ± 0.075	1.70 ± 0.25	*HST*	LBg	3
β Cet	111	−81	29.4 ± 0.7	18.36 ± 0.05	2.20 ± 0.55	*HST*	LBg	5
HR 1099	185	−41	29.0 ± 0.7	18.131 ± 0.020	1.46 ± 0.09	*HST*	LBg	5
σ Gem	191	23	37 ± 1	18.201 ± 0.037	1.36 ± 0.20	*HST*	LBg	1
WD 1634−573	330	−7	37 ± 3	18.85 ± 0.06	1.60 ± 0.25	*FUSE*	LBg	6
WD 2211−495	346	−53	53 ± 16	18.76 ± 0.15	1.51 ± 0.60	*FUSE*	LBg	7
HZ 43	54	84	68 ± 13	17.93 ± 0.03	1.66 ± 0.14	*FUSE*	LBg	8
G191-B2B	156	7	69 ± 15	18.18 ± 0.09	1.66 ± 0.45	*FUSE*	LBg	9
Feige 24	166	−50	74 ± 20	18.47 ± 0.03	1.3 ± 0.5	*HST*	LBg	10
WD 0621−376	245	−21	78 ± 23	18.70 ± 0.15	1.41 ± 0.56	*FUSE*	LBg	11
GD 246	87	−45	79 ± 24	19.110 ± 0.025	$1.51^{+0.20}_{-0.17}$	*FUSE*	LBg	12
α Vir	316	51	80 ± 6	19.00 ± 0.10	$1.6^{+1.6}_{-0.6}$	*Copernicus*	LBg	13
31 Com	115	89	94 ± 8	17.88 ± 0.03	2.0 ± 0.2	*HST*	LBg	1
α Cru	300	0	98 ± 6	19.60 ± 0.10	$2.5^{+0.7}_{-0.9}$	*Copernicus*	...	13
BD +28°4211	82	−19	104 ± 18	19.85 ± 0.02	1.39 ± 0.10	*FUSE*	...	14
θ Car	290	−5	135 ± 9	20.28 ± 0.10	0.50 ± 0.16	*Copernicus*	...	15
β CMa	226	−14	153 ± 15	18.20 ± 0.16	$1.2^{+1.1}_{-0.5}$	*Copernicus*	LBg	16
β Cen	312	1	161 ± 15	19.54 ± 0.05	$1.26^{+1.25}_{-0.45}$	*Copernicus*	...	13
Feige 110	74	−59	179^{+265}_{-67}	$20.14^{+0.07}_{-0.10}$	2.14 ± 0.41	*FUSE*	...	17
γ Cas	124	−2	188 ± 20	20.04 ± 0.04	1.12 ± 0.25	*Copernicus*	...	18
λ Sco	352	−2	216 ± 42	19.28 ± 0.03	0.76 ± 0.25	*Copernicus*	...	19
γ^2 Vel	263	−8	258 ± 35	19.710 ± 0.026	$2.18^{+0.22}_{-0.19}$	IMAPS	...	20
δ Ori	204	−18	281 ± 65	20.193 ± 0.025	$0.74^{+0.12}_{-0.09}$	IMAPS	...	21
μ Col	237	−27	397 ± 87	19.90 ± 0.10	$0.63^{+1.00}_{-0.23}$	*Copernicus*	...	13
ι Ori	210	−20	407 ± 127	20.16 ± 0.10	$1.4^{+0.5}_{-1.0}$	*Copernicus*	...	22
ϵ Ori	205	−17	412 ± 154	20.40 ± 0.08	0.65 ± 0.30	*Copernicus*	...	22
ζ Pup	256	−5	429 ± 94	19.963 ± 0.026	$1.42^{+0.15}_{-0.14}$	IMAPS	...	20
LS 1274	277	−5	580 ± 100	20.98 ± 0.04	0.76 ± 0.18	*FUSE*	LDg	23
JL 9	323	−27	590 ± 160	20.78 ± 0.05	1.00 ± 0.19	*FUSE*	LDg	23
HD 195965	86	5	794 ± 200	20.950 ± 0.025	$0.85^{+0.17}_{-0.12}$	*FUSE*	LDg	24
HD 191877	62	−6	2200 ± 550	21.05 ± 0.05	$0.78^{+0.26}_{-0.13}$	*FUSE*	LDg	24

[a] Quoted uncertainties assumed to be 1 σ (see text).
[b] Indicates which lines of sight are used to compute the gas-phase Local Bubble (LBg) and gas-phase local disk (LDg) D/H values described in the text.

REFERENCES.—(1) Dring et al. 1997; (2) Linsky et al. 1995; (3) Wood et al. 1996; (4) Wood et al. 2000; (5) Piskunov et al. 1997; (6) Wood et al. 2002; (7) Hébrard et al. 2002; (8) Kruk et al. 2002; (9) Lemoine et al. 2002; (10) Vennes et al. 2003; (11) Lehner et al. 2002; (12) Oliveira et al. 2003; (13) York & Rogerson 1976; (14) Sonneborn et al. 2002; (15) Allen et al. 1992; (16) Gry et al. 1985; (17) Friedman et al. 2002; (18) Ferlet et al. 1980; (19) York 1983; (20) Sonneborn et al. 2000; (21) Jenkins et al. 1999; (22) Laurent et al. 1979; (23) This paper; (24) Hoopes et al. 2003.

either 1 or 2 σ, but many others do not. Gaussian statistics are not necessarily applicable to D/H analyses, depending on the method used, and as a consequence the quoted uncertainties cannot precisely be given a "1 σ" or "2 σ" label. An example is the global fit approach described in § 4.1, which yields uncertainties that cannot be easily labeled "1 σ" or "2 σ," although we have argued that they can be considered close to "2 σ." (However, note that the Owens.f analysis also used here *does* compute formal Gaussian statistical uncertainties.) In any case, we follow McCullough's (1992) example of generally assuming that *Copernicus* uncertainties are 1 σ, but for many of the *HST* measurements without a clear definition of the quoted uncertainties, we assume that they are 2 σ. We return to this issue below. Note that for WD 0621−376 and WD 2211−495 we have followed the example of Moos et al. (2002) in assuming 40% errors for log N(H I) and D/H.

In Figure 6 the D/H values are plotted versus distance and H I column density. There appears to be a strong tendency for the D/H ratio to be low at the longest distances and the highest column densities. Of the 17 D/H measurements for lines of sight over 100 pc, there are only two that are greater than the gas-phase Local Bubble value of $(D/H)_{LBg} \approx 1.5 \times 10^{-5}$ (Linsky 1998), while 15 are lower. The apparent dependence of D/H on distance and N(H I) is strengthened considerably by the addition of the two new D/H data points from the JL 9 and LS 1274 lines of sight, which are both lengthy, high column density lines of sight with low values of D/H. Figure 6*b* has been divided into three column density regimes: log N(H I) < 19.2, 19.2 < log N(H I) < 20.5, and log N(H I) > 20.5. The D/H ratio appears constant in the lowest and highest regimes, although at different values, while D/H appears to be variable in the intermediate region. A similar dependence was found

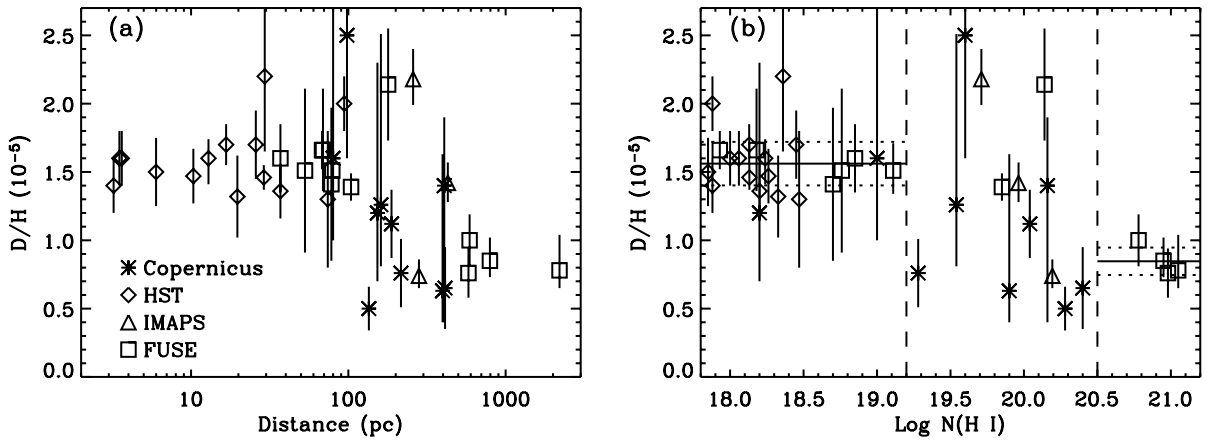

FIG. 6.—(*a*) D/H vs. line-of-sight distance, using the D/H measurements listed in Table 4. Different symbols are used for different sources of the D I measurement. (*b*) D/H vs. line-of-sight H I column density. The symbols are the same as in (*a*). D/H appears to be constant for $\log N(\mathrm{H\ I}) < 19.2$ and for $\log N(\mathrm{H\ I}) > 20.5$, but with different values of $\mathrm{D/H} = (1.56 \pm 0.16) \times 10^{-5}$ and $\mathrm{D/H} = (0.85 \pm 0.10) \times 10^{-5}$, respectively. These weighted means and 1 σ standard deviations are shown in the figure. For intermediate values of $19.2 < \log N(\mathrm{H\ I}) < 20.5$ D/H appears to be variable.

by Hébrard & Moos (2003) for the D/O and D/N ratios. The apparent variability of D/H beyond 100 pc has been noted previously (Jenkins et al. 1999; Moos et al. 2002; Hébrard & Moos 2003; Linsky 2004). These results can be explained if the gas-phase D/H in the ISM is variable on some well-defined size scale, with regions of constant D/H having a typical column density of $\log N(\mathrm{H\ I}) \sim 19$ (like the Local Bubble). However, very long sight lines sample many of these regions, so the D/H variations should average out for sufficiently lengthy lines of sight. Thus, for $\log N(\mathrm{H\ I}) \gtrsim 20.5$ we once again start to see roughly constant D/H.

We consider the lowest column density regime in Figure 6*b* to be that of the Local Bubble, and D/H here is consistent with a constant value of $(\mathrm{D/H})_{\mathrm{LBg}} = (1.56 \pm 0.16) \times 10^{-5}$ (1 σ standard deviation). The 22 lines of sight from which this $(\mathrm{D/H})_{\mathrm{LBg}}$ value is computed are flagged with "LBg" in the second to last column of Table 4. It is worth noting that 3 out of the 22 LBg D/H measurements have error bars that do not overlap the average $(\mathrm{D/H})_{\mathrm{LBg}}$ value. This is a reasonable fraction for 1 σ error bars, which is an a posteriori argument for the quoted error bars in Table 4 being reasonably accurate. If the error bars were increased significantly, the agreement with the average $(\mathrm{D/H})_{\mathrm{LBg}}$ value would look *too* good. Given the apparent constancy of $(\mathrm{D/H})_{\mathrm{LBg}}$, it is appropriate to replace the standard deviation error with a standard deviation of the mean, so our final value for the Local Bubble gas-phase D/H is $(\mathrm{D/H})_{\mathrm{LBg}} = (1.56 \pm 0.04) \times 10^{-5}$.

The constancy of both D/H and D/O within the Local Bubble is known from previous work, and our new $(\mathrm{D/H})_{\mathrm{LBg}}$ value is in good agreement with previous Local Bubble measurements (Linsky 1998, 2004; Moos et al. 2002; Hébrard & Moos 2003). This homogeneity of local gas-phase D/H values likely results from gas within the Local Bubble being well mixed, with a common history initiated by supernova events and O star winds emerging from the Sco-Cen association a few million years ago. The D/H values within the Local Bubble are indicative of conditions in its warm clouds, which have similar ages and chemical compositions and are bathed in similar UV radiation fields. Note that Hébrard & Moos (2003) derive a value of $(\mathrm{D/H})_{\mathrm{LBg}} = (1.32 \pm 0.08) \times 10^{-5}$ from D/O and a typical ISM O/H ratio, and they discuss possible reasons why this value does not agree precisely with the direct D/H measurements.

The high column density boundary where D/H becomes roughly constant again is somewhat unclear, but in Figure 6*b* we draw it at $\log N(\mathrm{H\ I}) = 20.5$, corresponding to a distance of $d \approx 500$ pc. There are four D/H measurements with larger columns, which are flagged with "LDg" in Table 4. All of these measurements are from *FUSE* (including the two new ones presented here). We believe that these long lines of sight provide the best measurements of the local disk gas-phase D/H ratio, $(\mathrm{D/H})_{\mathrm{LDg}}$, since they sample far more regions of the ISM than do shorter lines of sight with lower columns. However, with only four measurements we cannot rule out the possibility that other Galactic lines of sight with similarly high columns might exist that yield significantly different D/H. The Feige 110 [$\log N(\mathrm{H\ I}) = 20.14^{+0.07}_{-0.10}$] and γ^2 Vel [$\log N(\mathrm{H\ I}) = 19.710 \pm 0.026$] lines of sight illustrate this possibility clearly, as both have D/H twice as high as that seen for the four $\log N(\mathrm{H\ I}) > 20.5$ sight lines. The α Cru D/H value is also high, but with very large error bars. Despite this, the tendency for high column density lines of sight to yield low D/H seems substantial, considering that 14 of the 17 measurements with $\log N(\mathrm{H\ I}) > 19.2$ have $\mathrm{D/H} < (\mathrm{D/H})_{\mathrm{LBg}}$.

Collectively, the four $\log N(\mathrm{H\ I}) > 20.5$ lines of sight suggest $(\mathrm{D/H})_{\mathrm{LDg}} = (0.85 \pm 0.10) \times 10^{-5}$ (1 σ standard deviation). Since the four D/H measurements are individually consistent with this value, we can assume constancy and replace the 1 σ error quoted above with a standard deviation of the mean, as we did for $(\mathrm{D/H})_{\mathrm{LBg}}$, thereby obtaining a final value of $(\mathrm{D/H})_{\mathrm{LDg}} = (0.85 \pm 0.09) \times 10^{-5}$. This can be compared to the $(\mathrm{D/H})_{\mathrm{LDg}} = (0.52 \pm 0.09) \times 10^{-5}$ result found by Hébrard & Moos (2003) for long distances from D/O measurements combined with O/H from Meyer et al. (1998), and it agrees even better with their $(\mathrm{D/H})_{\mathrm{LDg}} = (0.86 \pm 0.13) \times 10^{-5}$ result similarly derived from D/N measurements and N/H from Meyer et al. (1997).

In the past, the well-determined Local Bubble D/H value, $(\mathrm{D/H})_{\mathrm{LBg}}$, has been assumed to be characteristic of the Galaxy as a whole, but D/H measurements for long lines of sight suggest that $(\mathrm{D/H})_{\mathrm{LBg}}$ is *not* representative of the Galactic ISM and that the Local Bubble D/H value is actually a factor of 2 higher than the true average gas-phase local disk D/H value. However, is the total (i.e., gas plus dust) local disk D/H ratio [$(\mathrm{D/H})_{\mathrm{LD}}$] equal to the gas-phase value [$(\mathrm{D/H})_{\mathrm{LDg}}$], or could the Local Bubble value [$(\mathrm{D/H})_{\mathrm{LBg}}$] actually be a better estimate

for $(D/H)_{LD}$? The answer depends on the cause of the D/H variability seen in Figure 6, which we now discuss in some detail.

5.2. *What is the Cause of the* D/H *Variability?*

5.2.1. *Variable Astration*

Possible causes for the D/H variability have been previously discussed by Lemoine et al. (1999) and Moos et al. (2002). One explanation for the D/H variability apparent in Figure 6 is that the ISM is simply not well mixed on distance scales of a few hundred parsecs and column density scales of $19.2 < \log N(\mathrm{H\ I}) < 20.5$, despite being relatively homogeneous on smaller and larger scales. If this is the case, different ISM regions may be characterized by different amounts of stellar processing (i.e., astration), and this could therefore explain the observed D/H variations. Supernovae are the primary drivers of ISM mixing on large distance scales, although paradoxically they are also potential sources of abundance inhomogeneity. The degree of mixing in the Galactic ISM has been studied by hydrodynamic models of the ISM (e.g., de Avillez & Mac Low 2002). For the current Galactic supernova rate, it is found that mixing timescales are of order 350 Myr. Thus, the local ISM would not have a constant D/H if sources of inhomogeneities, mainly supernovae, have occurred within this timescale. The conclusion is that inhomogeneities can potentially exist in the local ISM, although their existence is by no means certain.

Arguments against this have been made based on measurements of O/H, which find no significant spatial variations (Meyer et al. 1998; André et al. 2003). However, these particular analyses only sample lines of sight with high column densities of $20.15 < \log N(\mathrm{H\ I}) < 21.5$, and based on Figure 6*b* we are now arguing that D/H may not vary in this high column density regime either. It is only at shorter distance scales with smaller columns that variability is apparent.

In the variable astration scenario, the long distance, high column density $(D/H)_{LDg} = (0.85 \pm 0.09) \times 10^{-5}$ value derived above would provide the best estimate for $(D/H)_{LD}$. This suggests a significantly greater degree of astration than has been previously assumed. When compared with $(D/H)_{prim}$ (see § 1), our $(D/H)_{LDg}$ value implies a deuterium destruction factor of 3.3 ± 0.6. This higher destruction factor might be a problem for Galactic chemical evolution models, since most models can account for destruction factors of only 1.5–3 (Prantzos 1996; Tosi et al. 1998; Chiappini et al. 2002). However, there are nonstandard models involving prominent Galactic winds that lead to significantly higher destruction factors (e.g., Vangioni-Flam & Cassé 1995; Scully et al. 1997).

5.2.2. *Depletion of Deuterium onto Dust Grains*

We can assume $(D/H)_{LD} = (D/H)_{LDg}$ only if deuterium is not significantly depleted onto dust preferentially to hydrogen. However, it has been argued that D *can* be preferentially depleted in this manner. Jura (1982) first suggested that cold interstellar grains could remove a significant amount of deuterium from the gas phase. Draine (2004) recently showed that extreme enrichments of deuterium in carbonaceous grains in the diffuse ISM are thermodynamically favored. The zero-point energy of the C−D bond exceeds that of the C−H bond by 0.092 eV, whereas the zero-point energy of the H−D bond exceeds that of the H−H bond by 0.035 eV. Thus, in thermodynamic equilibrium carbonaceous dust grains can have deuterium enrichments by a factor of greater than 10^4 for grain temperatures $T_{grain} < 70$ K. Large polycyclic aromatic hydrocarbon (PAH) molecules can also be highly deuterium enriched if they are as cold as the grains (Peeters et al. 2004). Under these conditions, the abundance of deuterium in the gas phase of the ISM would be reduced by 1×10^{-5}, which is sufficient to explain the low values of D/H for the lines of sight with large column densities.

Is this model of variable depletion of deuterium from the gas phase realistic given the dynamics and radiation environment of the ISM? Cold interstellar gas in clouds is known to have molecules with deuterium enrichment by factors of 10^4 or larger (e.g., Bacmann et al. 2003). It is unlikely that the lines of sight to JL 9 and LS 1274 traverse very much cold gas since the molecular hydrogen fractions are 0.056 and 0.032, respectively (see § 4.3.6). It is interesting, however, that the temperatures of the H_2 gas for these lines of sight are 89 ± 6 and 64 ± 5 K, sufficiently low for highly deuterated molecules to form. A more relevant consideration is the presence of dust grains even in warm gas, as indicated by metal depletions for short lines of sight in the Local Bubble. Given the low gas density of the diffuse ISM, cold grains coexist with warm ($T \approx 7000$ K) gas.

These considerations lead to the following possible explanation for the three D/H regimes shown in Figure 6*b*. Strong shocks produced by supernovae and the winds of hot stars evaporate grains, forcing all of the matter into the gas phase. Over time this gas cools, forming grains that, as they cool, preferentially remove deuterium from the gas phase. Lines of sight traversing regions that were recently shocked should have most or all of the material in the gas phase and thus the highest D/H ratio. The Local Bubble is one such region. Gas-phase D/H in the Local Bubble is likely close to $(D/H)_{LD}$, since there are only a few lines of sight (e.g., α Cru, Feige 110, and γ^2 Vel) with slightly higher gas-phase D/H values. The unusual, high D/H values for these few lines of sight may indicate that they pass through regions that were shocked more recently than the Local Bubble, or considering the small number of these high D/H results, they could just be statistical anomalies. Lines of sight with high column densities [$\log N(\mathrm{H\ I}) > 20.5$] likely traverse a statistical average of the Galactic disk material, consisting mostly of gas that has not been shocked for a long time and thus with low gas-phase D/H. The intermediate regime with $19.2 < \log N(\mathrm{H\ I}) < 20.5$, containing a wide variety of gas-phase values of D/H, does not contain a reasonable statistical average of shocked and unshocked gas along the individual lines of sight.

In this scenario, the Local Bubble value of $(D/H)_{LBg} = (1.56 \pm 0.04) \times 10^{-5}$ is a better estimate for $(D/H)_{LD}$ than the global gas-phase $(D/H)_{LDg}$ value computed from high column density lines of sight in § 5.1. However, the existence of a few lines of sight with $D/H > 2 \times 10^{-5}$ suggests that deuterium might even be slightly depleted within the Local Bubble, so if dust depletion is the cause of the D/H variations, we can only really say $(D/H)_{LD} \gtrsim (D/H)_{LBg}$. Perhaps future studies of interstellar dust grains collected within the solar system could provide a direct determination of the degree of deuterium depletion in the Local Bubble (Frisch et al. 1999). In any case, the deuterium destruction factor of 1.8 ± 0.3 suggested by the Local Bubble D/H value is much easier for Galactic chemical evolution models to explain than the higher destruction factor of 3.3 ± 0.6 implied by the variable astration scenario in § 5.2.1.

6. SUMMARY

We have analyzed *FUSE* observations of interstellar absorption for two long lines of sight toward the sdO stars JL 9 and LS 1274. Our results are summarized as follows:

1. Using two separate measurement techniques, we have measured column densities for many different atomic species and for the $J = 0$–5 rotational levels of H_2. The results are listed in Table 3.

2. We find low molecular fractions of $f(H_2) = 0.056 \pm 0.012$ and $f(H_2) = 0.032 \pm 0.006$ toward JL 9 and LS 1274, respectively. The H_2 gas along these lines of sight is found to have a temperature of $T = 89 \pm 6$ K for JL 9 and $T = 64 \pm 5$ K for LS 1274, both very typical values for H_2 in the Galaxy.

3. The D/H ratios for the two lines of sight are $D/H = (1.00 \pm 0.37) \times 10^{-5}$ for JL 9 and $D/H = (0.76 \pm 0.36) \times 10^{-5}$ for LS 1274 (2 σ uncertainties). These D/H values are low compared to the Local Bubble value. When considered with other measurements, these new results provide additional crucial evidence that long lines of sight with high column densities tend to have low gas-phase deuterium abundances. This confirms the results of Hébrard & Moos (2003) based on D/O and D/N measurements and older published D/H values.

4. We consider our two new D/H measurements in combination with previous Galactic D/H measurements from *Copernicus*, *HST*, IMAPS, and *FUSE*. Collectively, these data suggest that D/H is constant for both low column density [$\log N(\mathrm{H\ I}) < 19.2$] and high column density [$\log N(\mathrm{H\ I}) > 20.5$] lines of sight but variable for intermediate columns [$19.2 < \log N(\mathrm{H\ I}) < 20.5$]. This suggests that regions of constant D/H in the ISM have typical column densities of $\log N(\mathrm{H\ I}) \sim 19$. However, no variability is seen for lines of sight with $\log N(\mathrm{H\ I}) > 20.5$, perhaps as a result of the sampling of a large number of these regions for such long sight lines.

5. The low column density regime [$\log N(\mathrm{H\ I}) < 19.2$] represents the Local Bubble. Our gas-phase Local Bubble D/H value of $(D/H)_{LBg} = (1.56 \pm 0.04) \times 10^{-5}$ is consistent with previous measurements (Linsky 1998, 2004; Moos et al. 2002). The apparent constancy of D/H at high column densities relies heavily on the two new D/H values for JL 9 and LS 1274. Since longer, higher column density lines of sight sample more regions of the ISM, we argue that the D/H values for these longer lines of sight provide better estimates of the true gas-phase local disk D/H ratio [$(D/H)_{LDg}$] than the Local Bubble measurements. For the lines of sight with $\log N(\mathrm{H\ I}) > 20.5$ we find $(D/H)_{LDg} = (0.85 \pm 0.09) \times 10^{-5}$. This is a factor of 2 lower than $(D/H)_{LBg}$ but is similar to the value derived by Hébrard & Moos (2003) from D/O and D/N measurements of lengthy sight lines. [Note that errors quoted above for $(D/H)_{LBg}$ and $(D/H)_{LDg}$ are 1 σ standard deviations of the mean.]

6. The cause of the observed D/H variability within the Galaxy is uncertain. We discuss two possible explanations: (1) variable astration and incomplete mixing in the ISM, and (2) depletion of deuterium onto dust grains. If scenario 2 is correct, then the low D/H values measured for long lines of sight are due to depletion. In this case, the total (i.e., gas plus dust) D/H ratio of the local disk, $(D/H)_{LD}$, is at least as high as the Local Bubble value of $(D/H)_{LBg} = (1.56 \pm 0.04) \times 10^{-5}$ instead of being at the low gas-phase value of $(D/H)_{LDg} = (0.85 \pm 0.09) \times 10^{-5}$. However, if scenario 1 is correct, then $(D/H)_{LD} = (D/H)_{LDg}$. Deuterium destruction factors can be computed by comparing the Galactic and primordial D/H ratios. Scenario 1 suggests a destruction factor of 3.3 ± 0.6, while scenario 2 suggests a value of 1.8 ± 0.3. The latter is more consistent with the predictions of Galactic chemical evolution models.

This work is based on data obtained for the Guaranteed Time Team by the NASA-CNES-CSA *FUSE* mission operated by the Johns Hopkins University. Financial support to US participants has been provided by NASA contract NAS5-32985. This research has made use of the SIMBAD database, operated at CDS, Strasbourg, France. G. H. was supported by CNES. This work used the profile fitting procedure Owens.f developed by M. Lemoine and the French *FUSE* Team. G. H. would like to thank B. Godard for his help in data processing.

REFERENCES

Abgrall, H. A., Roueff, E., Launay, F., Roncin, J.-Y., & Subtil, J.-L. 1993a, A&AS, 101, 273
———. 1993b, A&AS, 101, 323
Allen, M. M., Jenkins, E. B., & Snow, T. P. 1992, ApJS, 83, 261
André, M. K., et al. 2003, ApJ, 591, 1000
Bacmann, A., Lefloch, B., Ceccarelli, C., Steinacker, J., Castets, A., & Loinard, L. 2003, ApJ, 585, L55
Black, J. H., & Dalgarno, A. 1973, ApJ, 184, L101
Boesgaard, A. M., & Steigman, G. 1985, ARA&A, 23, 319
Burles, S., Nollett, K. M., & Turner, M. S. 2001, ApJ, 552, L1
Chiappini, C., Renda, A., & Matteucci, F. 2002, A&A, 395, 789
de Avillez, M. A., & Mac Low, M.-M. 2002, ApJ, 581, 1047
Diplas, A., & Savage, B. D. 1994, ApJS, 93, 211
Draine, B. T. 2004, in Origin and Evolution of the Elements, ed. A. McWilliam & M. Rauch (Pasadena: Carnegie Obs.), 320
Dreizler, S. 1993, A&A, 273, 212
Dring, A. R., Linsky, J., Murthy, J., Henry, R. C., Moos, W., Vidal-Madjar, A., Audouze, J., & Landsman, W. 1997, ApJ, 488, 760
Ferlet, R., Vidal-Madjar, A., Laurent, C., & York, D. G. 1980, ApJ, 242, 576
Friedman, S. D., et al. 2002, ApJS, 140, 37
Frisch, P. C., et al. 1999, ApJ, 525, 492
Gry, C., York, D. G., & Vidal-Madjar, A. 1985, ApJ, 296, 593
Hébrard, G., & Moos, H. W. 2003, ApJ, 599, 297
Hébrard, G., et al. 2002, ApJS, 140, 103
Hoopes, C. G., Sembach, K. R., Hébrard, G., Moos, H. W., & Knauth, D. C. 2003, ApJ, 586, 1094
Howk, J. C., Sembach, K. R., Roth, K. C., & Kruk, J. W. 2000, ApJ, 544, 867
Jaidee, S., & Lyngå, G. 1974, Ark. Astron., 5, 345
Jenkins, E. B., Tripp, T. M., Wozniak, P. R., Sofia, U. J., & Sonneborn, G. 1999, ApJ, 520, 182
Jura, M. 1982, in Advances in Ultraviolet Astronomy, ed. Y. Kondo (NASA CP-2238; Washington: NASA), 54
Kilkenny, D., Heber, U., & Drilling, J. S. 1988, South African Astron. Obs. Circ., 12, 1
Kirkman, D., Tytler, D., Suzuki, N., O'Meara, J. M., & Lubin, D. 2003, ApJS, 149, 1
Kruk, J. W., et al. 2002, ApJS, 140, 19
Lallement, R., Ferlet, R., Lagrange, A. M., Lemoine, M., & Vidal-Madjar, A. 1995, A&A, 304, 461
Lallement, R., Welsh, B. Y., Vergely, J. L., Crifo, F., & Sfeir, D. 2003, A&A, 411, 447
Laurent, C., Vidal-Madjar, A., & York, D. G. 1979, ApJ, 229, 923
Lehner, N., Gry, C., Sembach, K. R., Hébrard, G., Chayer, P., Moos, H. W., Howk, J. C., & Désert, J.-M. 2002, ApJS, 140, 81
Lemoine, M., et al. 1999, NewA, 4, 231
———. 2002, ApJS, 140, 67
Levshakov, S. A., Dessauges-Zavadsky, M., D'Odorico, S., & Molaro, P. 2002, ApJ, 565, 696
Linsky, J. L. 1998, Space Sci. Rev., 84, 285
———. 2004, in Origin and Evolution of the Elements, ed. A. McWilliam & M. Rauch (Pasadena: Carnegie Obs.), 35

Linsky, J. L., Diplas, A., Wood, B. E., Brown, A., Ayres, T. R., & Savage, B. D. 1995, ApJ, 451, 335
Lubowich, D. A., Pasachoff, J. M., Balonek, T. J., Millar, T. J., Tremonti, C., Roberts, H., & Galloway, R. P. 2000, Nature, 405, 1025
McCullough, P. R. 1992, ApJ, 390, 213
Meyer, D. M., Cardelli, J. A., & Sofia, U. J. 1997, ApJ, 490, L103
Meyer, D. M., Jura, M., & Cardelli, J. A. 1998, ApJ, 493, 222
Moos, H. W., et al. 2000, ApJ, 538, L1
———. 2002, ApJS, 140, 3
Morton, D. C. 2003, ApJS, 149, 205
Oliveira, C. M., Hébrard, G., Howk, J. C., Kruk, J. W., Chayer, P., & Moos, H. W. 2003, ApJ, 587, 235
O'Meara, J. M., Tytler, D., Kirkman, D., Suzuki, N., Prochaska, J. X., Lubin, D., & Wolfe, A. M. 2001, ApJ, 552, 718
Peeters, E., Allamandola, L. J., Bauschlicher, C. W., Jr., Hudgins, D. M., Sandford, S. A., & Tielens, A. G. G. M. 2004, ApJ, 604, 252
Pettini, M., & Bowen, D. V. 2001, ApJ, 560, 41
Piskunov, N., Wood, B. E., Linsky, J. L., Dempsey, R. C., & Ayres, T. R. 1997, ApJ, 474, 315
Prantzos, N. 1996, A&A, 310, 106
Rachford, B. L., et al. 2001, ApJ, 555, 839
———. 2002, ApJ, 577, 221
Romano, D., Tosi, M., Matteucci, F., & Chiappini, C. 2003, MNRAS, 346, 295
Sahnow, D. J., et al. 2000, ApJ, 538, L7
Savage, B. D., Bohlin, R. C., Drake, J. F., & Budich, W. 1977, ApJ, 216, 291
Scully, S., Cassé, M., Olive, K. A., & Vangioni-Flam, E. 1997, ApJ, 476, 521
Sembach, K. R., et al. 2004, ApJS, 150, 387
Sfeir, D. M., Lallement, R., Crifo, F., & Welsh, B. Y. 1999, A&A, 346, 785
Snow, T. P., et al. 2000, ApJ, 538, L65
Snowden, S. L., Egger, R., Finkbeiner, D. P., Freyberg, M. J., & Plucinsky, P. P. 1998, ApJ, 493, 715
Sonneborn, G., Tripp, T. M., Ferlet, R., Jenkins, E. B., Sofia, U. J., Vidal-Madjar, A., & Wozniak, P. R. 2000, ApJ, 545, 277
Sonneborn, G., et al. 2002, ApJS, 140, 51
Spitzer, L., Jr. 1978, Physical Processes in the Interstellar Medium (New York: Wiley)
Stephenson, C. B., & Sanduleak, N. 1971, Publ. Warner Swasey Obs., 1, 1
Thejll, P., Flynn, C., Williamson, R., & Saffer, R. 1997, A&A, 317, 689
Tosi, M., Steigman, G., Matteucci, F., & Chiappini, C. 1998, ApJ, 498, 226
Vangioni-Flam, E., & Cassé, M. 1995, ApJ, 441, 471
Vennes, S., Polomski, E. F., Lanz, T., Thorstensen, J. R., Chayer, P., & Gull, T. R. 2000, ApJ, 544, 423
Vidal-Madjar, A., Laurent, C., Bonnet, R. M., & York, D. G. 1977, ApJ, 211, 91
Wood, B. E., Alexander, W. R., & Linsky, J. L. 1996, ApJ, 470, 1157
Wood, B. E., Linsky, J. L., Hébrard, G., Vidal-Madjar, A., Lemoine, M., Moos, H. W., Sembach, K. R., & Jenkins, E. B. 2002, ApJS, 140, 91
Wood, B. E., Linsky, J. L., & Zank, G. P. 2000, ApJ, 537, 304
York, D. G. 1983, ApJ, 264, 172
York, D. G., & Rogerson, J. B. 1976, ApJ, 203, 378